ION ESCAPE FROM MARS

QI ZHANG

Licentiate Thesis

Main supervisor:
MATS HOLMSTRÖM

Assistant supervisors:
XIAO-DONG WANG
SHAHAB FATEMI
HANS NILSSON

Swedish Institute of Space Physics
Kiruna, Sweden

Department of Physics
Faculty of Science and Technology
Umeå University
Umeå, Sweden

May 2023

ISBN: 978-91-8070-100-6 (print)
ISBN: 978-91-8070-101-3 (pdf)
ISSN: 0284-1703
Printed by CityPrint i Norr AB
Umeå, Sweden 2023

ABSTRACT

When the solar wind reaches the Mars obstacle, mass loading by planetary ions slows down the solar wind and raises the bow shock. The Martian atmosphere is undergoing the a scavenging by the solar wind without the protection of a global magnetic field. Atmospheric escape is an important process for the evolution of the Martian climate. For present Mars, the dominant escape of atmospheric neutrals is through four channels: Jeans escape, photochemical reactions, sputtering and electron impact ionization. Ions above the exobase get accelerated by the solar wind electric field and can escape.

We here apply a new method for estimating heavy ion (O^+, O_2^+, and CO_2^+) escape rates at Mars, which combines a hybrid model and observations. We use observed upstream solar wind parameters as input for a hybrid plasma model, where the total ion upflux at the exobase is a free parameter. We then vary this ion upflux to find the best fit to the observed bow shock location. This method gives us a self-consistent description of the Mars-solar wind interaction, which can be used to study other properties of the solar wind interaction besides escape.

SAMMANFATTNING

När solvinden stöter på Mars så tyngs den ner av joner från planeten, vilket bromsar solvinden och expanderar bogshocken. Mars atmosfär eroderas av solvinden eftersom planeten saknar ett globalt magnetfält. Atmosfärsförlust är en viktig process i hur Mars klimat förändras. För nuvarande Mars är det fyra dominerande processer för förlust av neutrala atomer: Jeans förlust, fotokemiska reaktioner, sputtering och elektronkollisionsjonisering. Joner ovan exobasen accelereras av solvinden och kan förloras.
Här använder vi en ny metod för att uppskatta förlusten av tunga joner (O^+, O_2^+, and CO_2^+) vid Mars, som kombinerar en hybridmodell och observationer. Vi använder observerade solvindsparametrar som indata till en hybrid plasmamodell, där totalt jonuppflöde vid exobasen är en fri parameter. Vi varierar sedan detta jonuppflöde för att hitta bästa passningen till den observerade positionen för bogshocken. Metoden ger en självkonsistent beskrivning av Mars växelverkan med solvinden, som kan användas till att studera andra egenskaper av växelverkan, förutom jonförlust.

ACKNOWLEDGMENTS

This work was supported by The Swedish National Space Agency, Grant 198/19.
Computing resources used in this work were provided by the Swedish National Infrastructure for Computing (SNIC) at the High Performance Computing Center North (HPC2N), Umeå University, Sweden. The software used in this work was in part developed by the DOE NNSA-ASC OASCR Flash Center at the University of Chicago.
The ASPERA-3 electron data used, from the ELS sensor, is available in ESA's Planetary Science Archive (PSA) at
https://archives.esac.esa.int/psa/ftp/MARS-EXPRESS/ASPERA-3/
The MAVEN data used in this work, ion data from the SWIA instrument and magnetic field data from the MAG instrument, is available in University of Colorado Boulder Science Data Center at
https://lasp.colorado.edu/maven/sdc/public/data/sci/kp/

LIST OF APPENDED PAPERS

PAPER I

Zhang, Q., M. Holmström and X.D. Wang (2023). Effects of ion composition on escape and morphology at Mars. Submitted to Annales Geophysicae

PAPER II

Zhang, Q., M. Holmström, X.D. Wang, H. Nilsson and S. Barabash (2023). The influence of solar irradiation and solar wind conditions on heavy ion escape at Mars. Draft

CONTENTS

1 INTRODUCTION

Mars is the forth terrestrial planet from the sun. The orange-red appearance of Mars is due to the fact that its surface is covered with hematite. Mars is about half the diameter of Earth, and has a similar tilt and rotation period, but the sidereal period is as twice as Earth. The brightness of Mars can be -2.9 magnitude, but it is still dimmer than Jupiter most of the time. The thin and cold Martian atmosphere is dominated by carbon dioxide (95.3%). The atmospheric pressure is too low to maintain liquid water. The surface of Mars is full of impact craters, canyons, sand dunes, and gravel. The south hemisphere is an ancient, crater-filled plateau, while the north hemisphere is a younger, lowland plain. Mars does not have a global magnetic field. Instead, there's crustal magnetic fields in the south hemisphere. Mars has two moons, Phobos and Deimos. Both are irregularly shaped.

The in-situ exploration of Mars can be traced back to 1960s. More than 40 spacecrafts, including orbiters, landers and rovers, have been launched to study the Martian surface, geology and climate. So far, Mars has 13 spacecrafts in operation, including eight in the orbit: 2001 Mars Odyssey, Mars Express (MEX), Mars Reconnaissance Orbiter, Mars Atmosphere and Volatile Evolution (MAVEN), ExoMars Trace Gas Orbiter, the Hope orbiter, and the Tianwen-1 orbiter, and 5 on the surface: the Mars Science Laboratory Curiosity rover, the Perseverance rover, the Ingenuity helicopter, the Tianwen-1 lander, and the Zhurong rover.

Opportunity discovered the mineral jarosite on the surface of Mars (Elwood Madden, Bodnar, and Rimstidt, 2004). This is only formed in the presence of acidic water, suggesting that water was once present on Mars. Later, the Spirit rover found concentrated deposits of silica (Squyres et al., 2008), suggesting the wet weather in the past. If water has existed in the past, it makes people wonder how the water disappeared on Mars and how the climate evolved over time. Atmospheric escape is considered to be an vital mechanism of altering the Mars environment (Jakosky and Phillips, 2001; Jakosky et al., 2017; McKay and Stoker, 1989). This study is focusing on the process of ion escape and the role of the solar wind in the interaction with Mars.

2 THE SOLAR WIND INTERACTION WITH MARS

When the solar wind reaches the Mars obstacle, it is slowed down by the mass loading of the planetary ions, generating the bow shock, decelerated from supersonic to subsonic. The shocked solar wind plasma populates the hotter, denser and more turbulent magnetosheath. The magnetic field is highly draped in the magnetic pileup region (MPR), or induced magnetosphere (IM), where the planetary plasma is dominating and the solar wind plasma is barely observed. The MPR extended to the nightside and is connected to tail lobe region. The boundary between the magnetosheath and the MPR is called the magnetic pileup boundary (MPB), or induced magnetosphere boundary (IMB). Below the MPR, the photoelectron boundary (PEB) separates the cold local ions from the MPR. Inside the PEB planetary ions are abundant in the ionosphere. In the tail behind Mars, the two lobes are separated by the currents in the plasma sheet. The crustal fields in the south hemisphere makes the topology of the ionosphere more intricate than for a completely unmagnetized planet. Fig 2.1 depicts the structure created by the solar wind interaction with Mars.

2.1 BOW SHOCK

The Martian bow shock has been identified by earlier Mars missions, such as, Mariner 4 flyby (Smith et al., 1965), Mars 2, 3, 5 orbiters (Bogdanov and Vaisberg, 1975; Dolginov, Yeroshenko, and Zhuzgov, 1976; Gringauz et al., 1973) and the Phobos 2 orbiter (Riedler and al., 1989; Schwingenschuh et al., 1990). Later the bow shock variability has been studied by MGS (Vignes et al., 2002), MEX (Hall et al., 2016, 2019), and MAVEN (Garnier et al., 2022b). The structure of a the bow shock includes a foot, ramp, and overshoot. The magnitude of the overshoots is computed as $A = (B_M\text{-}B_2)/B_2$ (shown in Fig 2.2). The thickness of the overshoot (between the beginning of the shock foot and the minimum of the first undershoot) in most cases is between 0.5 and 2.5 of the solar wind proton gyroradius. Due to the small size of Mars and the weak IMF, the solar wind proton gyroradius is approximately of the same scale as the bow shock. In consequence, kinetic effects are important in the collisionless Martian bow shock (Lembège and Savoini, 2002). The location of the Martian bow shock at the subsolar point is at an altitude of $\sim 0.58\ R_M$ (Mars radius) and $\sim 1.6\ R_M$ at the terminator (Brain, 2006). The shape of the bow shock is asymmetric due to IMF direction, south hemisphere crustal field and planetary ion outflow.
The bow shock location shows strong dependency on the upstream con-

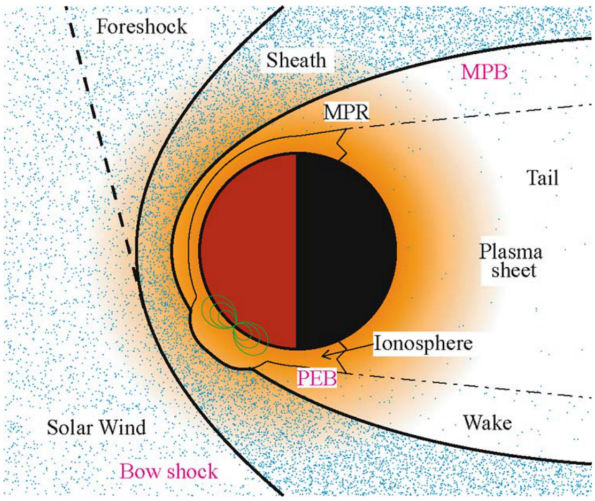

Figure 2.1: Sketch of the global Martian solar wind interaction according to Brain, 2006.

ditions. Fig 2.3 displays that the bow shock terminator distance increases as the solar EUV increases and the distance has the same tendency with respect to the solar cycle. Vignes et al., 2002 illustrated that the quasi-parallel shock is closer to the planet than the quasi-perpendicular shock and the bow shock terminator distance is greater for larger cone angles (the angle between the interplanetary magnetic field and the direction of the solar wind velocity). Hall et al., 2016 found that the bow shock terminator distance decreases as the solar wind dynamic pressure increases. Garnier et al., 2022a explained the significant influence of the crustal fields on the bow shock location and found that this influence varies with season.

2.2 MAGNETOSHEATH

In the magnetosheath region, at the beginning, protons are suddenly heated. Then the proton density and velocity drop and is gradually cooled down. Planetary ions start to arise and get accelerated. Since the magnetosheath region is only on the order of the solar wind proton gyroradius, there's not enough space for the solar wind plasma to get thermalized (Dubinin et al., 1993). The magnetic field is highly oscillating in the magnetosheath region. Ultra low frequency waves are abundant in this area, appearing 48% of the time (Bertucci et al., 2004). Mirror mode waves are generated from the temperature anisotropy in the particle distribution function in a high beta plasma (Hasegawa, 2012). These

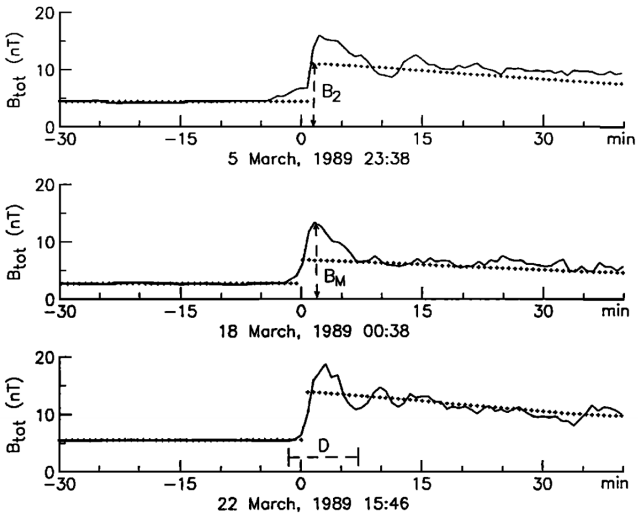

Figure 2.2: Magnetic field profiles of three bow shock crossing cases of Phobos 2 according to Tatrallyay et al., 1997. Continuous line, measured total field; dotted line, simulated values using MHD model. B_M is the maximum field value at the overshoot, B_2 is the calculated downstream field at the shock, and D is the apparent thickness of the overshoot along the spacecraft trajectory.

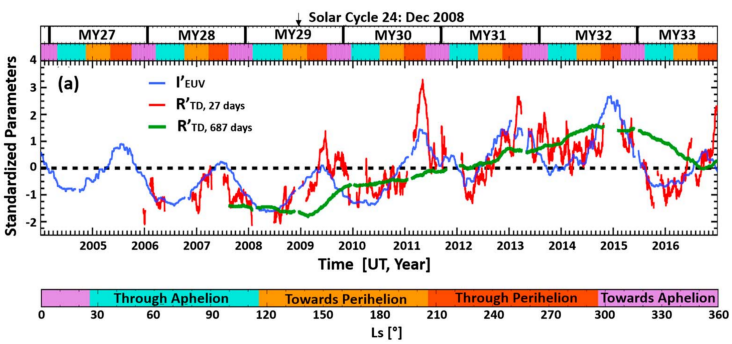

Figure 2.3: Bow shock variation with solar EUV and solar cycle according to Hall et al., 2019.

waves are found to be anticorrelated with the superthermal electron density.

2.3 MPB (IMB) AND MPR (IM) BOUNDARIES

The magnetic pileup boundary (or induced magnetosphere boundary) is formed and stop solar wind ions penetrating into the planet while the electrons carrying the magnetic field can go through it. MPB as the inner boundary for solar wind ions works similar to the magnetopause on Earth. The MPB is the result from the shocked solar wind interaction with planetary heavy ions. The main features of MPB are summarized as follows (Bertucci et al., 2011):

1. Magnetic field: sharp enhancement of the magnetic field draping, sharp increase in the magnetic field strength by a factor of 2–3, a drop in the magnetic field fluctuations.

2. Ion composition: decrease in the solar wind ion density accompanied by an increase of planetary ion density.

3. Electron: a sharp increase of the electron density, a drop in the electron temperature

Fig 2.4 shows an example of MPB boundary identification. At tha MPB, there's big jump in magnetic field strength (from ~ 10 nT to ~ 35 nT) and one order of magnitude drop in superthermal electron flux in less than 1 minute (or less than ~ 100 km). After the MPB, in the magnetic pileup region (or induced magnetosphere), θ (the elevation angle over Mars' orbital plane) is getting smooth and magnetic field is less oscillating.
Fig 2.5 depicts the measurements of two boundary crossings by MEX (Edberg et al., 2009a) and fittings by MGS (Edberg et al., 2008). The location of the Martian MPB at the subsolar point is at an altitude of ~ 0.33 R_M (Mars radius) and ~ 0.45 R_M at the terminator. Edberg et al., 2009a has done a parameter study of the MPB boundary variation. They found that the MPB and bow shock don't respond to upstream solar wind conditions or planetary condition in the same way. MPB terminator distance to the planet is negatively correlated to solar wind dynamic pressure and magnetic pressure. The stronger solar EUV flux causes the terminator MPB to move inward. The area with crustal field increases the MPB terminator distance compared to the area without.
The MPR has prominent drapping effects. The magnetic field is expected to be predominately horizontal (in the plane of the IMF). Fig 2.6 displays the correlation between $B_{x'}$ component and B_r component. In the magnetosheath region, the direction of the magnetic field is highly variable. $B_{x'}$ and B_r are not correlated. While in the MPR, the magnetic field becomes regular. $B_{x'}$ and B_r are roughly linearly related. This feature can be used to identify the MPR. In the MPR, the planetary plasma is dominant. It's also the primary region where the energy and momentum

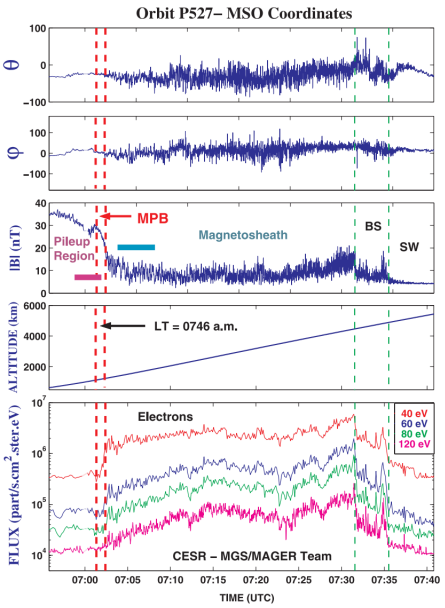

Figure 2.4: An example of MPB and bow shock crossing detected by MAG/ER for an orbit near the terminator plane in MSO coordinate according to Bertucci et al., 2003. θ is the elevation angle over Mars' orbital plane, ϕ is the azimuth (0° = sunward).

transfer happens from solar wind to Martian ions. On the dayside, the MPR is only a few hundred km thick (Bertucci et al., 2011). β (thermal pressure over magnetic pressure) is decreased in the MPR due to the high magnetic pressure and low thermal pressure from the cold planetary ions. Therefore the mirror mode is replaced by fast magnetosonic waves (Bertucci et al., 2004). In the magnetotail, the MPR is composed of two lobes separated by the plasma sheet.

2.4 PEB AND IONOSPHERE

Below the MPR, there's one more boundary separating the cold ionosphere from the highly-draped induced magnetosphere. In this boundary, the solar wind electrons are replaced by photoelectrons released by the neutral atmosphere absorbing solar EUV. This boundary is called the photoelectron boundary. Fig 2.7 shows the increased electron flux, but of decreased energy, after the PEB. Photoelectrons has also been observed in the MPR by vertical transport. Photoelectrons also can travel along the draped field lines to the nightside (Cui et al., 2015). The topology of the PEB is strongly affected by crustal fields (Brain et al., 2003).
The dayside ionosphere is maintained by photochemical reactions, form-

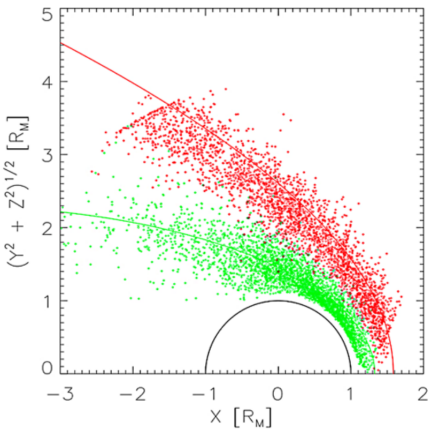

Figure 2.5: The position of the bow shock (red dots) and MPB (green dots) crossings by MEX according to Edberg et al., 2009a. The dashed lines are the boundaries fitting to MGS measurements according to Edberg et al., 2008.

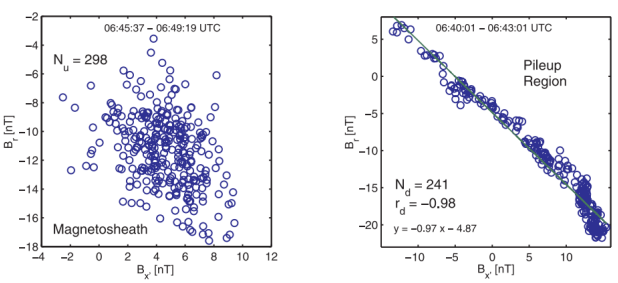

Figure 2.6: $B_{x'}$ versus B_r in the Martian magnetosheath (left panel), and in the MPR (right panel) of one MGS orbit according to Bertucci et al., 2003. B_r is the radial cylindrical component of B in y-z plane.

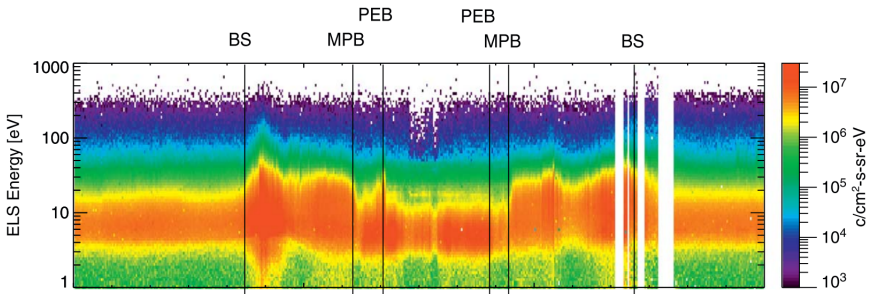

Figure 2.7: Electron energy spectrogram by MEX according to Edberg et al., 2009b.

ing a permanent structure. The distribution of the dayside ionosphere is following Chapman theory. The peak of the ionosphere is ~ 125 km (Nagy et al., 2004). While the nightside ionosphere is mostly from impact ionization by precipitating solar wind electrons (Safaeinili et al., 2007) and day-night transport of ions (Cui et al., 2015). 2.8 displays the morphology of the topside Martian ionosphere both on the dayside and nightside from MAVEN observations. O^+ and O_2^+ are the primary ion species in the ionosphere. The ion density appears to decline exponentially with increasing altitude. The electron density equals the total ion density.

2.5 CRUSTAL FIELDS

Mars does not have a global magnetic field. Instead there are many pockets of strong magnetism locked up in its crust, called crustal fields. The crustal fields has been discovered by the low periapsis of MGS. The magnitude of the strong crustal field in the south hemisphere is up to 1600 nT at ~ 100 km altitude, much higher than the strength of magnetic pile-up region (~ 30 nT). The reason for crustal field formation is still under investigation. One possible explanation is the sea-floor spreading in the presence of a reversing dynamo in the early era of plate tectonics (Connerney et al., 2005).

The structure of the magnetic field lines close to Mars is rather complicated. Three morphologies have been assumed: closed field lines with both feet ending in Mars, open field lines with one foot connecting to Mars and another foot connecting to IMF, and unconnected field lines both ending in IMF. Brain et al., 2003 found that reconnection between the solar wind and crustal fields takes place above 7% of the Martian surface. Fan et al., 2019 noticed that the planetary ions tend to be trapped in the crustal field region and this reduced global escape flux by nearly 35%. The nightside suprathermal electrons are found to be depleted strongly in the crustal field region beyond 170 km (Steckiewicz et al., 2017), meaning the crustal field prevents the solar wind electrons

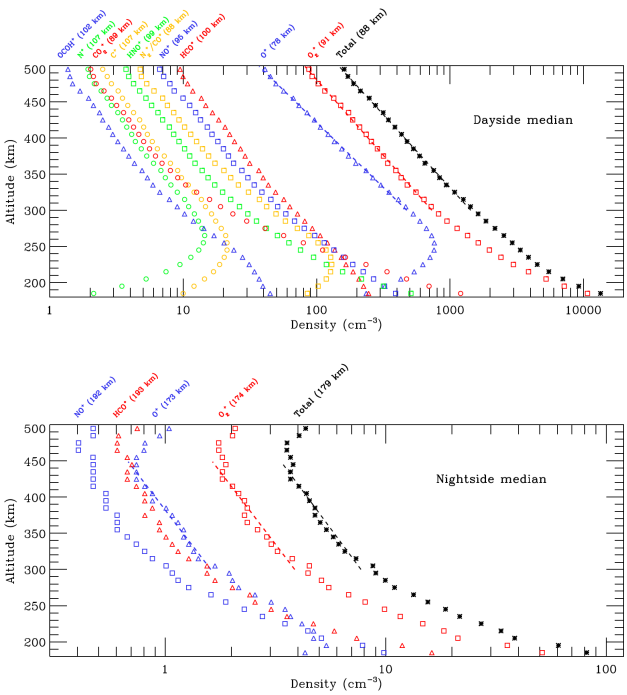

Figure 2.8: The profile of the main ion species on the dayside and nightside Martian ionosphere at an altitude of at 180–500 km according to Wu et al., 2019. The value in brackets represent the scale height of each ion specie.

from precipitating. Crustal fields also has a significant influence on the boundaries distance in a positive way (Vignes et al., 2000).

3 ATMOSPHERIC ESCAPE FROM MARS

The atmosphere of unmagnetized planets are exposed to the solar wind environment and lose particles by interacting directly with the solar wind mainly through two ways (Luhmann and Kozyra, 1991): heated by solar extreme ultraviolet (EUV), mostly the neutral atmosphere, and picked-up by solar wind flow, mostly the ions. Atmospheric escape is one of the consequences of the solar wind interaction with Mars.

3.1 NEUTRAL ESCAPE

3.1.1 *Jeans escape*

Jeans (or thermal) escape is likely the primary mechanism for hydrogen loss at Mars. In the upper atmosphere, H_2O undergoes photodissociation and produces H_2. H_2 is then further dissociated and generates atomic hydrogen. The escape energy of H at the exobase ($\sim$ 200 km) is only $\sim$ 0.1 eV. In the tail of the Maxwell-Boltzmann distribution, the energy is high enough for the light H atoms to overcome the gravity and escape to space.
The most common means of measuring H loss is by observing Lyman alpha light scattered H atoms in the thermosphere and corona (Chaffin et al., 2018). H escape is found to be 1-10 $\cdot 10^{26}$ s^{-1} (Bhattacharyya et al., 2015; Chaffin et al., 2018, 2014), depending on the assumed model temperature and season variation. High temperatures allow water vapor to be carried up to higher altitudes. During the Mars southern-summer season, the increased atmospheric dust is cooling down the atmosphere by absorbing the visible wavelength sunlight.

3.1.2 *Photochemical escape*

In general, the atomic O escape flux, F_{esc}, referred to the surface of Mars is determined by

$$F_{esc} = \frac{1}{R_M^2} \int (Z + R_M)^2 P_{hot}(Z) \epsilon_{esc}(Z) dZ, \tag{3.1}$$

where z is the altitude, R_M is the solid-body radius of Mars, P_{hot} is the hot O production rate, and ϵ_{esc} is the escape probability. When not stated explicitly, all flux values mentioned below refer to the surface.
The most extensively studied hot O production mechanism is O_2^+ Dissociative Recombination (DR) (Lillis et al., 2017), which may occur in two channels with the amount of kinetic energy release carried by O above

its local escape energy of 1.98 eV at an exobase altitude of 200 km (Fox and Hać, 2009) These two DR channels are

$$\begin{aligned} O_2^+ + e &\rightarrow O(^3P) + O(^3P) + 6.99eV, (a) \\ &\rightarrow O(^1D) + O(^3P) + 5.02eV, (b) \end{aligned} \tag{3.2}$$

where e denotes a thermal electron and the respective exothermicities are also provided. Here the hot O production rate could be calculated using the O_2^+ DR coefficient of Peverall et al., 2001 that depends on the thermal electron temperature, along with a branching ratio of 26.5% for channel (a) and 47.3% for channel (b), both assuming O_2^+ in the vibrational ground state (Petrignani et al., 2005). With MAVEN measurements and multiple escape probability models, they yield O atom loss estimates around $5{\cdot}10^{25}$ s^{-1} (Cravens et al., 2017; Lillis et al., 2017; Rahmati et al., 2017).

3.1.3 *Sputtering escape*

The planetary heavy ions picked up by the solar wind can precipitate and transfer energy to neutral oxygen in the upper atmosphere via elastic collisions. This process is called sputtering. It's efficient enough to accelerate a certain amount of atomic oxygen to escape (Luhmann, Johnson, and Zhang, 1992; Luhmann and Kozyra, 1991). The solar wind protons or alpha particles has less chance to contribute to sputtering escape due to the requirements for such light ions to sputter are very restrictive: the solar wind particles need to be above 1 keV near the exobase (Watson, Haff, and Tombrello, 1980), which is normally impossible. Since the sputtering is driven by the precipitating ions, it highly depends on the solar wind conditions.
The sputtering can not be detected directly. However the precipitating ion flux is possible to measure. Thereafter, models are used to simulate the collision process and estimate the escape caused by sputtering. Combing MAVEN ion flux observation and Exospheric General Model, Leblanc et al., 2018 gave an evaluation of sputtering escape rate on Mars as $4{\cdot}10^{23}$ s^{-1} and found that sputtering is the main O escape mechanism on the nightside.

3.1.4 *Electron impact escape*

CO_2 electron impact is recognized as a viable mechanism of neutral heating in the Martian upper atmosphere (Fox and Dalgarno, 1979) due to the abundant CO_2 source. These electron impact (EI) processes are capable of producing hot O atoms via the predissociation of CO_2 and CO_2^+ in electronically excited states (Zhang et al., 2020),

$$CO_2 + e^* \rightarrow O + CO^+ + 2e^*, \tag{3.3}$$

where e* denotes an energetic electron, either impacting or secondary. Energetic electrons are present in the Martian upper atmosphere due to solar EUV/X-ray ionization on the dayside or SW precipitation on the nightside. For such a process, a portion of the kinetic energy released is carried away by the neutral and ion fragments through ionization and excitation. An evaluation with the aid of the combined data sets accumulated by several instruments on board MAVEN reveals that CO_2 electron impact makes a non-negligible contribution to total atomic O escape on Mars, with a median escape rate of $\sim 10^{24}$ s^{-1} on the dayside and $\sim 10^{22}$ s^{-1} on the nightside (Zhang et al., 2020).

3.2 ION ESCAPE

The nascent Martian ions are too cold to escape gravity. They however get energized by the local electromagnetic field via different processes, including the movement of the solar wind ($-\mathbf{V} \times \mathbf{B}$), the magnetic shear stresses of the draped field lines ($\mathbf{J} \times \mathbf{B}$), plasma pressure gradients in the ionosphere (∇p_e) and plasma shear with the magnetic anomalies or plasma waves (C).

$$\mathbf{E} = -\mathbf{V} \times \mathbf{B} + \frac{1}{n_e e}\mathbf{J} \times \mathbf{B} - \frac{1}{n_e e}\nabla p_e + C \tag{3.4}$$

From measurements, Lundin et al., 1989 observed O^+ loss rate as $3{\cdot}10^{25}$ s^{-1} near solar maximum with Phobos 2. Barabash et al., 2007 derived ions escape rate for three species: O^+ as $1.6{\cdot}10^{23}$ s^{-1}, O_2^+ as $1.5{\cdot}10^{23}$ s^{-1} and CO_2^+ as $8{\cdot}10^{22}$ s^{-1} using ASPERA-3/Ion Mass Analyser data on MEX mission in the energy range of 30 eV to 30 keV. Dong et al., 2017 studied MAVEN Surpathermal and Thermal Ion Composition (STATIC) data and found >6 eV O^+ loss rate is $2{\cdot}10^{24}$ s^{-1} in the low EUV case and $3{\cdot}10^{24}$ s^{-1} in the high EUV case. With more than one solar cycle MEX data, Nilsson et al., 2021 interpolated the flux of lower energy ions and acquired heavy ions outflow at $1{\cdot}10^{25}$ s^{-1} in solar maximum and $2{\cdot}10^{24}$ s^{-1} in solar minimum. On the other hand, Ma and Nagy, 2007 calculated escape rate of three ion species (O^+, O_2^+, and CO_2^+) and found a variation from $2.7{\cdot}10^{23}$ s^{-1} to $2.4{\cdot}10^{24}$ s^{-1} depending on the upstream and planetary conditions, found with a multi-species MHD model. Ledvina et al., 2017 gave the value of ion loss rate at $1.2{\cdot}10^{25}$ s^{-1} with a hybrid model. Regoli et al., 2018 approximated a heavy ions total escape flux of $1.1{\cdot}10^{25}$ s^{-1} with a multi-fluid MHD model.

At Mars the escaping ionospheric ions usually form two major outflow channels: A cold fluid-like outflow in the tail behind the planet, and a more energetic outflow in the direction of solar wind convective electric field (Holmström and Wang, 2015). The escaping ions accelerated by the convective electric field $-\mathbf{V}_{SW} \times \mathbf{B}$, is usually called the ion plume at Mars. The Martian ion plume has been observed by MAVEN (Dong

et al., 2017, 2015; Dubinin et al., 2017) and MEX (Nilsson et al., 2021), and modeled by multifluid MHD (Dong et al., 2014; Ma et al., 2019; Regoli et al., 2018) and hybrid codes (Brecht, Ledvina, and Jakosky, 2017; Holmström and Wang, 2015). It is a matter of definition how to separate tail and plume fluxes, in observations and models. Dong et al., 2017 separated plume and tail flux by energy (>1 keV ions belong to the plume) and found that plume escape contributes 30% to total escape in low EUV conditions and 20% in high EUV conditions. Nilsson et al., 2021 defined the escape morphology using a geometric box and called the outflow perpendicular to the X-axis "radial escape". They found that the radial escape does not depend on the solar cycle, but that the highest radial escape occurs at high solar wind dynamic pressure conditions, and that the radial escape is around 20% to 40% of the total escape.

3.3 ATMOSPHERIC EVOLUTION

Mars is thought to be a warm and humid planet with thicker atmosphere ~ 3.5 billion years ago during the Noachian epoch (Jakosky and Phillips, 2001; Jakosky et al., 2017; McKay and Stoker, 1989) and is potentially able to host the life in the past. A few meters to a km scale ocean was likely existing (Boesswetter et al., 2010). The Martian atmospheric pressure at that period is estimated to be ~ 0.1 bar while it is ~ 6 mbar in the present. The atmospheric escape plays a significant role in the evolution of the previous thick to the current thin Mars atmosphere. The evolution of the sun of course affect the planetary escape process. To extrapolate earlier Mars loss process, it's necessary to reproduce earlier solar wind environment. The early sun has slower rotation rate (Newkirk Jr, 1980), accompanied by weaker IMF and stronger solar EUV flux and solar wind intensity. Several different models have been applied to evaluate the earlier Mars atmosphere escape rate (Chassefière et al., 2013; Dong et al., 2018; Lillis et al., 2017; Luhmann, Johnson, and Zhang, 1992; Ramstad et al., 2018). At present neutral escape is dominant. While in the past, ion escape is as vital as neutral escape, even more (Chassefière et al., 2013; Dong et al., 2018). Fig 3.1 shows the extrapolation result of photochemical O escape and ion escape over ancient time. It reveals 4 billion years ago, atmospheric escape is approximately 2-3 orders of magnitude larger than now.

The Martian dynamo is found to be shut down ~ 4 billion years ago (Lillis et al., 2013). In addition to the evolution of the sun, the change from the past global intrinsic magnetic field to current local crustal field possibly plays a part in the Martian atmosphere evolution. Sakai et al., 2018 introduced a weak global dipole magnetic field in a Mars MHD model and found 25% enhancement in the total ion escape rate compared to the magnetic anomalies case.

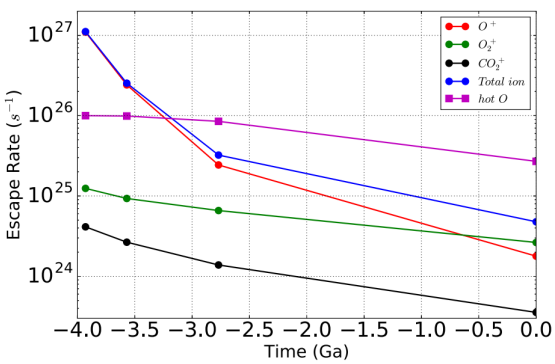

Figure 3.1: Martian atmosphere loss over time according to Dong et al., 2018.

4 MODELLING THE SOLAR WIND INTERACTION WITH MARS

Models are applied to simulate the global Mars plasma environment and the interaction with solar wind, from earlier gasdynamic models (Dryer and Heckman, 1967; Spreiter, Summers, and Rizzi, 1970) to present hybrid models (Brecht, Ledvina, and Jakosky, 2017; Holmström, 2010; Kallio et al., 2008; Modolo et al., 2016) and MHD models (Dong et al., 2014; Harnett and Winglee, 2006; Ma and Nagy, 2007; Regoli et al., 2018). In this study, a hybrid model is used to investigate the ion escape from the Martian atmosphere.

4.1 HYBRID MODEL

In a hybrid model, electrons are treated as a massless fluid and ions are treated as individual particles accelerated by the Lorentz force. Given the initial position $\mathbf{r_i}$ and velocity $\mathbf{v_i}$, the trajectories of the ions N_I are computed by,

$$\frac{d}{dt} = \mathbf{v_i}, \frac{d\mathbf{v_i}}{dt} = \frac{q_i}{m_i}(\mathbf{E} + \mathbf{v_i} \times \mathbf{B}), i = 1, 2, ..., N_I \tag{4.1}$$

where q_i is the ion charge [C] and m_i is the ion mass [kg]. By spatial averaging, we define the ion charge density ρ_I [Cm^{-3}] and average velocity $\mathbf{u_I}$ [m/s]. The ion current density $\mathbf{J_I} = \rho_I \mathbf{u_I}$ [$Cm^{-2}s^{-1}$]. A Hybrid model is charge neutral, $\rho_I + \rho_e = 0$, electron charge density $\rho_e = -\rho_I$. The total current $\mathbf{J} = \mathbf{J_I} + \mathbf{J_e}$ is computed by Ampère's law, from $\mathbf{B}$,

$$\mathbf{J} = \mu_0^{-1} \nabla \times \mathbf{B} \tag{4.2}$$

μ_0 is the vacuum permeability. The electric field is derived from Ohm's law,

$$\mathbf{E} = \frac{1}{\rho_I}(-\mathbf{J_I} \times \mathbf{B} + \mu_0^{-1}(\nabla \times \mathbf{B}) \times \mathbf{B} - \nabla p_e) + \frac{\eta}{\mu_0} \nabla \times \mathbf{B}, \tag{4.3}$$

where p_e is the electron pressure and η is the resistivity, respectively. The magnetic field is advanced in time by Faraday's law,

$$\frac{\partial \mathbf{B}}{\partial t} = -\nabla \times \mathbf{E} \tag{4.4}$$

The electric field can be basically divided into four terms: motional field, Hall field, ambipolar field and resistivity. Motional field $(-\mathbf{J_I} \times \mathbf{B})/\rho_I$,

that is to say, $-\mathbf{v_I} \times \mathbf{B}$, describes the electric field generated by the movement of the ions in the magnetic field. Hall field, $(-\mathbf{J} \times \mathbf{B})/\rho_I$, describes the electric field generated by the current. Ambipolar field comes from that the lighter electrons diffuse faster than ions and an electric field is generated in the direction against the density gradient. The ambipolar field in our model is derived from the negative gradient of the electron pressure, $p_e = n_e k T_e$.

4.2 MARS MODEL

In the study, we use Mars Solar Orbital (MSO) coordinates, where the origin is at the center of the planet, the X_{MSO}-axis is directed to the sun, the Y_{MSO}-axis is in the orbital plane, perpendicular to the X_{MSO}-axis, and opposite to Mars' motion. Then Z_{MSO}-axis completes the right-handed coordinate system. The cell size in the simulation is h =350 km. We have a spherical obstacle centered at the origin with a radius of 3550 km, representing the exobase. All ions inside the obstacle are removed from the simulation. The resistivity is $7{\cdot}10^5$ Ωm in a sphere of radius 3380 km representing the solid planet. Outside the planet the resistivity is $5{\cdot}10^4$ Ωm, in the ionosphere and the surrounding plasma. The vacuum regions are defined as the regions with a plasma density less than 1% of solar wind density and the resistivity in vacuum regions is 10^6 Ωm. The number of macro particles per cell at the inflow boundary (the $+X_{MSO}$ side of the simulation box) is 8 for protons, and 2 for alpha particles. The weight (number of real particles represented by one macro particle) of the ionospheric ion macro particles are set to the same weight as for protons. An exobase upflux is composed of 54% O^+, 39% O_2^+ and 7% CO_2^+. The heavy ions are produced on the dayside, drawn from a Maxwellian distribution with a temperature of 200 K. The exobase ion upflux decays from the the subsolar point to the terminator by the cosine of solar zenith angle (Holmström and Wang, 2015). Each produced heavy ion is then moved radially outward by a distance randomly drawn from $[0, h]$. We run the model until a steady state is reached, after approximately 500 seconds of simulation time (when the number of heavy ions in the simulation domain remains on average constant). We do not include any neutral corona in the model. We can however note that in our method, additional mass loading from photoionization of neutrals in the exosphere will be compensated for by larger heavy ion upflux at the exobase, to achieve the observed bow shock location.

4.3 MODEL ALGORITHM

Both measurements and models have been applied to study the escape of ionospheric ions, but each approach has limitations. For the detection by instruments on spacecrafts, it's difficult to cover all energies, especially

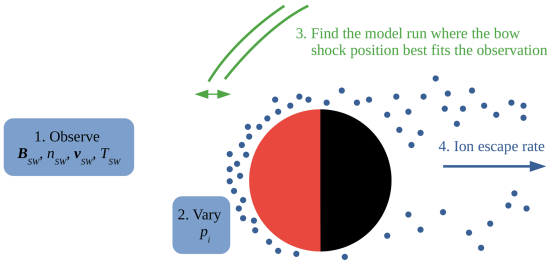

Figure 4.1: The sketch of algorithm according to Holmström, 2022.

low energies, and the full 4π sr field of view. Furthermore, an in-situ observation is only at a certain place and time. To cover all of the interaction region, we need to accumulate data for a long time and rely on statistics. Therefore, observing the complete interaction region at a specific time is impossible with a single spacecraft. Using simulations, we can get a full three-dimensional picture at any instance. Nevertheless, the ionosphere and atmosphere are highly dynamic and it's impossible to include all relevant physics in the models. Therefore, we here use a new method to take advantage of both measurements and models, by combing hybrid model and observations, to get a global coverage of data and to enable detailed studies of physical processes.
We use the amount of mass-loading of the solar wind as a free parameter to combine the model and observations. Mass-loading of the solar wind flow occurs wherever thermal ions are inserted into the flow. Mass loading by planetary ions slows down the solar wind and raises the bow shock (Alexander and Russell, 1985; Hall et al., 2016; Mazelle et al., 2004; Vignes et al., 2002). Given similar upstream conditions, the standoff distance of the bow shock from the planet will depend on the degree of mass-loading, which is dependent on the ion densities in the upper parts of the ionosphere. At Mars, heavy ions at the top of the ionosphere will provide the mass-loading, and wave-particle interactions will generate a bow shock in the colissionless solar wind plasma upstream of the planet (Szegö et al., 2000). We use observed upstream solar wind parameters as input for a hybrid plasma model, where the total ion upflux at the exobase is a free parameter. We then vary this ion upflux to find the best fit for the observed bow shock location. A motivation for having such a simplified ionosphere, represented by only one free parameter, is that the ionosphere is highly variable in time and space (Chaufray et al., 2015; Fowler et al., 2022; Leelavathi, Rao, and Rao, 2023), making the construction of an accurate ionospheric model difficult.

The algorithm is shown in Fig 4.1 :

1. We apply observed upstream solar wind parameters (solar wind density (with 5% of alpha particles), velocity, ion and electron temperatures, and magnetic field) at the inflow boundary. To

derive these parameters, we calculated their median values in the undisturbed solar wind with MAVEN Key Parameters file outside the nominal bow shock (Vignes et al., 2000).

2. Then we run several simulations with different heavy ion upflux rates at the exobase.

3. Next, we compare the simulation results with observations in magnetic field and the proton density, to find the simulation run that best fits the observed bow shock location. The space resolution of these observations is higher than for the model (the model cell size).

4. We can then derive an escape rate estimate from this best fit run. The total escape rate is computed by averaging the outflow in the region $X_{MSO} < -1.5R_m$ after reaching a steady state.

4.4 MODEL EXAMPLE

Here we give an example. We apply our method to one MAVEN orbit #811 occurring during 13:00 to 15:00 UTC on 1 March 2015. Table 4.1 displays the upstream solar wind conditions for this orbit from MAVEN observations. We run three simulations with three different total exobase upflux rates listed in Table 4.2. All the runs are with the same input upstream conditions listed in Table 4.1. The simulation results are then compared with MAVEN measurements of magnetic field, solar wind velocity and proton density in Fig 4.2.
By visual inspection, the Upflux 2 simulation fits the observation best. Upflux 1 gives a bow shock too close to the planet, since the upflux is too small, while Upflux 3 gives a bow shock too far away from the planet. We see a good agreement between the model and observations in the magnetosheath region (the grey area in Fig 4.2). Closer to the planet, below the Induced Magnetosphere Boundary (IMB), the model magnetic field is not increasing dramatically as the observation, where we do not expect the perfect fit due to the simplified ionosphere we use, and the lack of crustal magnetic fields in our model. We also verify the fit for the Upflux 2 simulation using MEX Electron Spectrometer (ELS) observations of bow shock crossings in Fig 4.3. This supports that Upflux 2 is the best fitting simulation run. We use the result of this simulation as the escape rate of orbit #811.

Table 4.1: Upstream solar wind parameters in MSO coordinates on 1 March 2015 estimated from MAVEN observations

Density [cm^{-3}]	2.4
Velocity [km/s]	(-350, 45, 12)
Proton temperature [K]	1.2×10^5
Electron temperature [K]	1.7×10^5
Interplanetary magnetic field [nT]	(-1, -2.7, -1)

Table 4.2: The total exobase ion upflux and resulting total escape rates for the three simulations

Case	O^+ [s^{-1}]	O_2^+ [s^{-1}]	CO_2^+ [s^{-1}]	Escape rate [s^{-1}]
Upflux 1	4.6×10^{24}	3.2×10^{24}	6.1×10^{23}	5.08×10^{24}
Upflux 2	5.0×10^{24}	3.6×10^{24}	6.7×10^{23}	6.78×10^{24}
Upflux 3	5.5×10^{24}	3.9×10^{24}	7.3×10^{23}	8.94×10^{24}

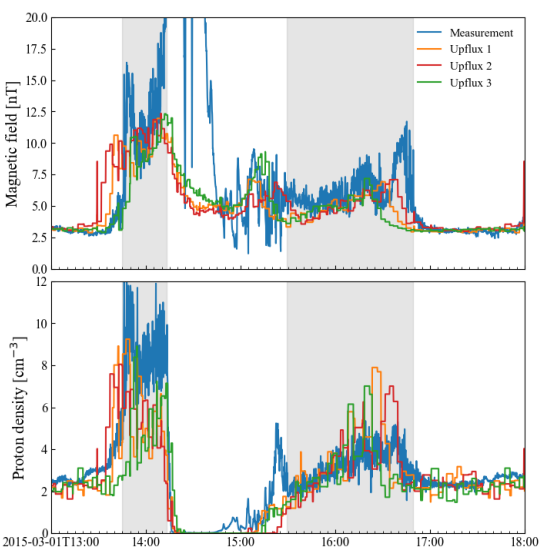

Figure 4.2: Model results compared to MAVEN measurements (blue lines). Orange, red and green lines are the simulation results for three different productions in Table 4.2, respectively. The plot shows a comparison for the magnetic field magnitude and the proton density. The bow shock location is identified by the change in magnetic field and solar wind density. The grey areas indicate the magnetosheath regions.

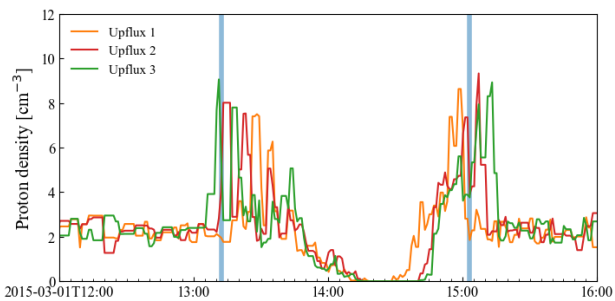

Figure 4.3: Model results of Table 4.2 compared to MEX measurements. Blue lines are bow shock crossing times from MEX ELS observations.

5 DISCUSSION OF RESULTS

We have applied the recent-proposed method (described in Section 4.3) to one MAVEN orbit (described in Section 4.4), to investigate the effects on ion escape estimates of assumed heavy ion composition in the ionosphere, alpha particles in the solar wind, solar wind velocity aberration and electron temperature. We find that the ion compositions at the exobase with larger mass leads to a smaller estimate of the escape rate. The escape estimate is inversely proportional to the square root of the atomic mass of the escaping ion specie. We also find that the assumed fraction, and temperature, of alpha particles in the upstream solar wind, have a positive effect on escape estimates. The effect of solar wind aberration on escape rate of that orbit is found to be 7% and it's basically from the change in the convective electric field. In addition, we notice that the escape rate is sensitive to the assumed upstream electron temperature and increases with it.

We thereafter investigate some parameters and how they have an effect on Martian ion escape withe same model described in Section 4.3. First we looked at the upstream conditions. The model results show that the escape rate is higher in high EUV. The total escape rate in solar maximum is 2-4 times of solar minimum. This is because more ions produced during solar maximum resulting in the larger escape. We find that the solar wind dynamic pressure has positive effect on ion escape. One hypothesis is the energy transfer is more efficient in higher solar wind dynamic pressure case. Another hypothesis is that the tail flux is energized by the compression of the magnetic tail current in stronger dynamic pressure. Moreover, the heavy ion loss is reducing when the IMF strength is increasing. Larger IMF strength drives stronger magnetic pile-up in front of the planet and generates a thicker and stronger induced magnetosphere, which protects the atmosphere from escaping. We also find that when solar wind velocity is parallel to the IMF, the escape rate is highest. When they are perpendicular, the escape rate is lowest. Finally and counterintuitively, our result indicates the plume escape is decreasing as the solar wind convective field is increasing.

In the future, we will study the other type of factors that are potentially affecting the ion loss on Mars, planetary condition, like dust storms and the crustal magnetic fields. Also it will be of interest to study extreme upstream condition cases, such as, Coronal Mass Ejection (CME) events and radial cases (when the solar wind is parallel to IMF).

6 SUMMARY OF PAPERS

PAPER I

Zhang, Q., M. Holmström and X.D. Wang (2023). Effects of ion composition on escape and morphology at Mars. Submitted to Annales Geophysicae

In this paper, we refine a recently presented method to estimate ion escape from non-magnetized planets and apply it to Mars. The method combines in-situ observations and a hybrid plasma model (ions as particles, electrons as a fluid). We use measurements from the Mars Atmosphere and Volatile Evolution Mission and Mars Express for one orbit on 2015-03-01. Observed upstream solar wind conditions are used as input to the model. We then vary the total ionospheric ion upflux until the solution fits the observed bow shock location. We find that estimates of total heavy ion escape are not very sensitive to the composition of the heavy ions, or the amount and temperature of the solar wind alpha particles. We also find that velocity aberration has a minor influence on escape, but that it is sensitive to the solar wind electron temperature. The plume escape is found to contribute 29% of the total heavy ion escape, in agreement with observations. Heavier ions have a larger fraction of escape in the plume compared to the tail. We also find that the escape estimates scales inversely with the square root of the atomic mass of the escaping ion specie.

PAPER II

Zhang, Q., M. Holmström, X.D. Wang, H. Nilsson and S. Barabash (2023). The influence of solar irradiation and solar wind conditions on heavy ion escape at Mars. Draft

This paper is based on the method developed in the first paper and further discusses about how upstream conditions, including solar Extreme Ultraviolet (EUV), solar wind dynamic pressure, Interplanetary Magnetic Field (IMF) strength and cone angle, affect the heavy ions loss on Mars. The results indicate that the heavy ions escape rate is higher in high EUV. The ion escape rate increases as solar wind dynamic pressure increases. The ion escape rate decreases as solar wind IMF strength increases. The ion escape rate is highest when the solar wind is parallel to the IMF while lowest when the solar wind is perpendicular to the

IMF. The plume escape is decreasing when the convective electric field is increasing.

BIBLIOGRAPHY

Alexander, C. J. and C. T. Russell (1985). "Solar cycle dependence of the location of the Venus bow shock." In: *Geophysical research letters* 12.6, pp. 369–371.

Barabash, S., A. Fedorov, R. Lundin, and J. A. Sauvaud (2007). "Martian atmospheric erosion rates." In: *Science* 315.5811, pp. 501–503.

Bertucci, C., F. Duru, N. Edberg, M. Fraenz, C. Martinecz, K. Szego, and O. Vaisberg (2011). "The induced magnetospheres of Mars, Venus, and Titan." In: *Space science review* 162, pp. 113–171.

Bertucci, C., C. Mazelle, D. H. Crider, D. L. Mitchell, K. Sauer, M. H. Acuña, ..., and D. Winterhalter (2004). "MGS MAG/ER observations at the magnetic pileup boundary of Mars: Draping enhancement and low frequency waves." In: *Advances in Space Research* 33.11, pp. 1938–1944.

Bertucci, C., C. Mazelle, D. H. Crider, D. Vignes, M. H. Acuña, D. L. Mitchell, ..., and D. Winterhalter (2003). "Magnetic field draping enhancement at the Martian magnetic pileup boundary from Mars global surveyor observations." In: *Geophysical research letters* 30.2.

Bhattacharyya, D., J. T. Clarke, J. L. Bertaux, J. Y. Chaufray, and M. Mayyasi (2015). "A strong seasonal dependence in the Martian hydrogen exosphere." In: *Geophysical Research Letters* 42, 8678–8685.

Boesswetter, A., H. Lammer, Y. Kulikov, U. Motschmann, and S. Simon (2010). "Non-thermal water loss of the early Mars: 3D multi-ion hybrid simulations." In: *Planetary and Space Science* 58.14-15, pp. 2031–2043.

Bogdanov, A. V. and O. L. Vaisberg (1975). "Structure and variations of solar wind-Mars interaction region." In: *Journal of Geophysical Research* 80.4, 487–494.

Brain, D. A. (2006). "Mars Global Surveyor measurements of the Martian solar wind interaction." In: *Space Science Reviews* 126, pp. 77–112.

Brain, D. A., F. Bagenal, M. H. Acuña, and J. E. P. Connerney (2003). "Martian magnetic morphology: Contributions from the solar wind and crust." In: *Journal of Geophysical Research: Space Physics* 108.A12.

Brecht, Stephen H., Stephen A. Ledvina, and Bruce M. Jakosky (2017). "The role of the electron temperature on ion loss from Mars." In: *Journal of Geophysical Research: Space Physics* 122.8, pp. 8375–8390.

Chaffin, M. S., J. Y. Chaufray, J. Deighan, N. M. Schneider, M. Mayyasi, J. T. Clarke, ..., and B. M. Jakosky (2018). "Mars H escape rates derived from MAVEN/IUVS Lyman alpha brightness measurements and their dependence on model assumptions." In: *Journal of Geophysical Research: Planets* 123.8, pp. 2192–2210.

Chaffin, M. S., J. Y. Chaufray, I. Stewart, F. Montmessin, N. M. Schneider, and J. L. Bertaux (2014). "Unexpected variability of Martian hydrogen escape." In: *Geophysical Research Letter* 41, 314–320.

Chassefière, E., B. Langlais, Y. Quesnel, and F. Leblanc (2013). "The fate of early Mars' lost water: the role of serpentinization." In: *Journal of Geophysical Research: Planets* 118.5, pp. 1123–1134.

Chaufray, J. Y., F. Gonzalez-Galindo, F. Forget, Lopez-Valverde, M. A., F. Leblanc, R. Modolo, and S. Hess (2015). "Variability of the hydrogen in the Martian upper atmosphere as simulated by a 3D atmosphere–exosphere coupling." In: *Icarus* 245, pp. 282–294.

Connerney, J. E. P., M. H. Acuña, N. F. Ness, G. Kletetschka, D. L. Mitchell, R. P. Lin, and H. Rème (2005). "Tectonic implications of Mars crustal magnetism." In: *Proceedings of the National Academy of Sciences of the United States of America* 102.42, 14970–14975.

Cravens, T. E., A. Rahmati, J. L. Fox, R. Lillis, S. Bougher, J. Luhmann, ..., and B. Jakosky (2017). "Hot oxygen escape from Mars: Simple scaling with solar EUV irradiance." In: *Journal of Geophysical Research: Space Physics* 122.1, pp. 1102–1116.

Cui, J., M. Galand, R. V. Yelle, Y. Wei, and S. J. Zhang (2015). "Day-to-night transport in the Martian ionosphere: Implications from total electron content measurements." In: *Journal of Geophysical Research* 120.3, 2333–2346.

Dolginov, S. S., Y. G. Yeroshenko, and L. N. Zhuzgov (1976). "The magnetic field of Mars according to the data from the Mars 3 and Mars 5." In: *Journal of Geophysical Research* 81.19, 3353–3362.

Dong, C., S. W. Bougher, Y. Ma, G. Toth, A. F. Nagy, and D. Najib (2014). "Solar wind interaction with Mars upper atmosphere: Results from the one-way coupling between the multifluid MHD model and the MTGCM model." In: *Geophysical Research Letters* 41.8, pp. 2708–2715.

Dong, C., Y. Lee, Y. Ma, M. Lingam, S. Bougher, J. Luhmann, ..., and B. Jakosky (2018). "Modeling Martian atmospheric losses over time: implications for exoplanetary climate evolution and habitability." In: *The Astrophysical Journal Letters* 859.1, p. L14.

Dong, Y., X. Fang, D. A. Brain, J. P. McFadden, J. S. Halekas, J. E. P. Connerney, F. Eparvier, L. Andersson, D. Mitchell, and B. M. Jakosky (2017). "Seasonal variability of Martian ion escape through the plume and tail from MAVEN observations." In: *Journal of Geophysical Research: Space Physics* 122.4, pp. 4009–4022.

Dong, Y., X. Fang, D. A. Brain, J. P. McFadden, J. S. Halekas, J. E. Connerney, ..., and B. M. Jakosky (2015). "Strong plume fluxes at Mars observed by MAVEN: An important planetary ion escape channel." In: *Geophysical Research Letters* 42.21, pp. 8942–8950.

Dryer, M. and G.R. Heckman (1967). "Application of the hypersonic analog to the standing shock of Mars." In: *Sol Phys* 2, 112–124.

Dubinin, E., R. Lundin, H. Koskinen, and O. Norberg (1993). "Cold ions at the Martian bow shock: Phobos observations." In: *Journal of Geophysical Research: Space Physics* 98.A4, pp. 5617–5623.

Dubinin, E. et al. (2017). "The Effect of Solar Wind Variations on the Escape of Oxygen Ions From Mars Through Different Channels: MAVEN Observations." In: *Journal of Geophysical Research: Space Physics* 122.11, 11,285–11,301.

Edberg, N. J. T., D. A. Brain, M. Lester, S. W. H. Cowley, R. Modolo, M. Fränz, and S. Barabash (2009a). "Plasma boundary variability at Mars as observed by Mars Global Surveyor and Mars Express." In: *Annales Geophysicae. Göttingen, Germany: Copernicus Publications* 27.9, pp. 3537–3550.

Edberg, N. J. T., M. Lester, S. W. H. Cowley, and A. I. Eriksson (2008). "Statistical analysis of the location of the Martian magnetic pileup boundary and bow shock and the influence of crustal magnetic fields." In: *Journal of Geophysical Research: Space Physics* 113.A8.

Edberg, N. J., A. I. Eriksson, U. Auster, S. Barabash, A. Bößwetter, C. M. Carr, ..., and J. G. Trotignon (2009b). "Simultaneous measurements of Martian plasma boundaries by Rosetta and Mars Express." In: *Planetary and Space Science* 57.8-9, pp. 1085–1096.

Elwood Madden, M. E., R. J. Bodnar, and J. D. Rimstidt (2004). "Jarosite as an indicator of water-limited chemical weathering on Mars." In: *Nature* 431.7010, pp. 821–823.

Fan, K., M. Fraenz, Y. Wei, Q. Han, E. Dubinin, J. Cui, ..., and J. E. P. Connerney (2019). "Reduced atmospheric ion escape above Martian crustal magnetic fields." In: *Geophysical Research Letters* 46.21, pp. 11764–11772.

Fowler, C. M., J. McFadden, K. G. Hanley, D. L. Mitchell, S. Curry, and B. Jakosky (2022). "In-Situ Measurements of Ion Density in the Martian Ionosphere: Underlying Structure and Variability Observed by the MAVEN-STATIC Instrument." In: *Journal of Geophysical Research: Space Physics* 127.8, e2022JA030352.

Fox, J. L. and A. Dalgarno (1979). "Ionization, luminosity, and heating of the upper atmosphere of Mars." In: *Journal of Geophysical Research* 84.A12, p. 7315.

Fox, J. L. and A. B. Hać (2009). "Photochemical escape of oxygen from Mars: A comparison of the exobase approximation to a Monte Carlo method." In: *Icarus* 204.2, pp. 527–544.

Garnier, P., C. Jacquey, X. Gendre, V. Génot, C. Mazelle, X. Fang, ..., and J. S. Halekas (2022a). "The Influence of Crustal Magnetic Fields on the Martian Bow Shock Location: A Statistical Analysis of MAVEN and Mars Express Observations." In: *Journal of Geophysical Research: Space Physics* 127.5, e2021JA030146.

Garnier, P., C. Jacquey, X. Gendre, V. Génot, C. Mazelle, X. Fang, ..., and J. S. Halekas (2022b). "The drivers of the Martian bow shock location: A statistical analysis of Mars Atmosphere and Volatile EvolutioN

and Mars Express observations." In: *Journal of Geophysical Research: Space Physics* 127.5, e2021JA030147.

Gringauz, K., V. Bezrukikh, G. Volkov, T. Breus, I. Musatov, L. Havkin, and G. Sloutchonkov (1973). "Preliminary results on plasma electrons from Mars-2 and Mars-3." In: *Icarus* 18.1, 54–58.

Hall, B. E. S., B. Lester M.and Sánchez-Cano, J. D. Nichols, D. J. Andrews, N. J. Edberg, ..., and R. Orosei (2016). "Annual variations in the Martian bow shock location as observed by the Mars Express mission." In: *Journal of Geophysical Research: Space Physics* 121.11, pp. 11–474.

Hall, B. E. S., B. Sánchez-Cano, J. A. Wild, M. Lester, and M. Holmström (2019). "The Martian bow shock over solar cycle 23–24 as observed by the Mars Express mission." In: *Journal of Geophysical Research: Space Physics* 124.6, pp. 4761–4772.

Harnett, E. M. and R. M. Winglee (2006). "Three-dimensional multifluid simulations of ionospheric loss at Mars from nominal solar wind conditions to magnetic cloud events." In: *Journal of Geophysical Research: Space Physics* 111.A9.

Hasegawa, A. (2012). "Plasma instabilities and nonlinear effects." In: *Springer Science Business Media*.

Holmström, M. (2022). "Estimating ion escape from unmagnetized planets." In: *Annales Geophysicae. Copernicus GmbH* 40.1, pp. 83–89.

Holmström, M. (2010). "Hybrid modeling of plasmas." In: *Numerical Mathematics and Advanced Applications 2009: Proceedings of ENUMATH 2009, the 8th European Conference on Numerical Mathematics and Advanced Applications, Uppsala, July 2009. Berlin, Heidelberg: Springer Berlin Heidelberg*, pp. 451–458.

Holmström, M. and X. D. Wang (2015). "Mars as a comet: Solar wind interaction on a large scale." In: *Planetary and Space Science* 119, pp. 43–47.

Jakosky, B. M. and R. J. Phillips (2001). "Mars' volatile and climate history." In: *Nature* 412.6843, p. v.

Jakosky, B. M., M. Slipski, M. Benna, P. Mahaffy, M. Elrod, R. Yelle, ..., and N. Alsaeed (2017). "Mars' atmospheric history derived from upper-atmosphere measurements of 38Ar/36Ar." In: *Science* 355.6332, pp. 1408–1410.

Kallio, E., A. Fedorov, E. Budnik, S. Barabash, R. Jarvinen, and P. Janhunen (2008). "On the properties of O^+ and O_2^+ ions in a hybrid model and in Mars Express IMA/ASPERA-3 data: A case study." In: *Planetary and Space Science* 56.9, pp. 1204–1213.

Leblanc, F., A. Martinez, J. Y. Chaufray, R. Modolo, T. Hara, J. Luhmann, ..., and B. Jakosky (2018). "On Mars's atmospheric sputtering after MAVEN's first Martian year of measurements." In: *Geophysical Research Letters* 45.10, pp. 685–4691.

Ledvina, S. A., S. H. Brecht, D. A. Brain, and B. M. Jakosky (2017). "Ion escape rates from Mars: Results from hybrid simulations compared

to MAVEN observations." In: *Journal of Geophysical Research: Space Physics* 122.8, pp. 8391–8408.

Leelavathi, V., N. V. Rao, and S. V. B. Rao (2023). "Gravity wave driven variability in the Mars ionosphere-thermosphere system." In: *Icarus* 115430.

Lembège, B. and P. Savoini (2002). "Formation of reflected electron bursts by the nonstationarity and nonuniformity of a collisionless shock front." In: *Journal of Geophysical Research: Space Physics* 107.A3, SMP–X.

Lillis, R. J., J. Deighan, J. L. Fox, S. W. Bougher, Y. Lee, M. R. Combi, ..., and J. Y. Chaufray (2017). "Photochemical escape of oxygen from Mars: First results from MAVEN in situ data." In: *Journal of Geophysical Research: Space Physics,* 122.3, pp. 3815–3836.

Lillis, R. J., S. Robbins, M. Manga, J. S. Halekas, and H. V. Frey (2013). "Time history of the Martian dynamo from crater magnetic field analysis." In: *Journal of Geophysical Research: Planets* 118.7, pp. 1488–1511.

Luhmann, J. G., R. E. Johnson, and M. H. G Zhang (1992). "Evolutionary impact of sputtering of the Martian atmosphere by O^+ pickup ions." In: *Geophysical Research Letters* 19.21, 2151–2154.

Luhmann, J. G. and J. U. Kozyra (1991). "Dayside pickup oxygen ion precipitation at Venus and Mars: Spatial distributions, energy deposition and consequences." In: *Journal of Geophysical Research: Space Physics* 96.A4, pp. 5457–5467.

Lundin, R., A. Zakharov, R. Pellinen, H. Borg, B. Hultqvist, N. Pissarenko, ..., and H. Koskinen (1989). "First measurements of the ionospheric plasma escape from Mars." In: *Nature* 341.6243, pp. 609–612.

Ma, Y. J., C. F. Dong, G. Toth, B. van der Holst, A. F. Nagy, C. T. Russell, ..., and B. M. Jakosky (2019). "Importance of ambipolar electric field in driving ion loss from Mars: Results from a multifluid MHD model with the electron pressure equation included." In: *Journal of Geophysical Research: Space Physics* 124.11, pp. 9040–9057.

Ma, Y. J. and A. F. Nagy (2007). "Ion escape fluxes from Mars." In: *Geophysical Research Letters* 34.8.

Mazelle, C., D. Winterhalter, K. Sauer, J. G. Trotignon, M. H. Acuna, K. Baumgärtel, ..., and J. Slavin (2004). "Bow shock and upstream phenomena at Mars." In: *Space Science Reviews* 111.1, pp. 115–181.

McKay, C. P. and C. R. Stoker (1989). "The early environment and its evolution on Mars: Implication for life." In: *Reviews of Geophysics* 27.2, pp. 189–214.

Modolo, R., S. Hess, M. Mancini, F. Leblanc, J. Y. Chaufray, D. Brain, ..., and C. Mazelle (2016). "Mars-solar wind interaction: LatHyS, an improved parallel 3-D multispecies hybrid model." In: *Journal of Geophysical Research: Space Physics* 121.7, pp. 6378–6399.

Nagy, A. F., D. Winterhalter, K. Sauer, T. E. Cravens, S. Brecht, C. Mazelle, ..., and J. G. Trotignon (2004). "The plasma environment of Mars." In: *Mars' magnetism and its interaction with the solar wind*, pp. 33–114.

Newkirk Jr, G. (1980). "Solar variability on time scales of 10 to the 5th years to 10 to the 9.6 th years." In: *In The Ancient Sun: Fossil Record in the Earth, Moon and Meteorites*, pp. 293–320.

Nilsson, H., Q. Zhang, G. S. Wieser, M. Holmström, S. Barabash, Y. Futaana, ..., and M. Wieser (2021). "Solar cycle variation of ion escape from Mars." In: *Icarus* 114610.

Petrignani, A., W. J. van der Zande, P. C. Cosby, F. Hellberg, R. D. Thomas, and M. Larsson (2005). "Vibrationally resolved rate coefficients and branching fractions in the dissociative recombination of O_2^+." In: *The Journal of chemical physics* 122.1, p. 014302.

Peverall, R., S. Rosén, J. R. Peterson, M. Larsson, A. Al-Khalili, L. Vikor, ..., and W. J. van der Zande (2001). "Dissociative recombination and excitation of O_2^+: Cross sections, product yields and implications for studies of ionospheric airglows." In: *The Journal of Chemical Physics* 114.15, pp. 6679–6689.

Rahmati, A., D. E. Larson, T. E. Cravens, R. J. Lillis, J. S. Halekas, J. P. McFadden, ..., and B. M. Jakosky (2017). "MAVEN measured oxygen and hydrogen pickup ions: Probing the Martian exosphere and neutral escape." In: *Journal of Geophysical Research: Space Physics* 122.3, pp. 3689–3706.

Ramstad, R., S. Barabash, Y. Futaana, H. Nilsson, and M. Holmström (2018). "Ion Escape From Mars Through Time: An Extrapolation of Atmospheric Loss Based on 10 Years of Mars Express Measurements." In: *Journal of Geophysical Research: Planets* 123.11, pp. 3051–3060.

Regoli, L. H., Y. Ma C. Dong, E. Dubinin, W. B. Manchester, S. W. Bougher, and D. T. Welling (2018). "Multispecies and Multifluid MHD Approaches for the Study of Ionospheric Escape at Mars." In: *Journal of Geophysical Research: Space Physics* 123.9, pp. 7370–738.

Riedler, W. and et al. (1989). "Magnetic fields near Mars: First results." In: *Nature* 341.6243, 604–607.

Safaeinili, A., W. Kofman, J. Mouginot, Y. Gim, A. Herique, A. B. Ivanov, ..., and G. Picardi (2007). "Estimation of the total electron content of the Martian ionosphere using radar sounder surface echoes." In: *Geophysical Research Letters* 34.23.

Sakai, S., K. Seki, N. Terada, H. Shinagawa, T. Tanaka, and Y. Ebihara (2018). "Effects of a weak intrinsic magnetic field on atmospheric escape from Mars." In: *Geophysical Research Letters* 45.18, pp. 9336–9343.

Schwingenschuh, K., W. Riedler, H. Lichtenegger, Y. Yeroshenko, K. Sauer, J. G. Luhmann, M. Ong, and C. T. Russell (1990). "Martian bow shock: PHOBOS observations." In: *Geophysical Research Letters* 17.6, 889–892.

Smith, E. J., L. Davis, P. J. Coleman, and D. E. Jones (1965). "Magnetic field measurements near Mars." In: *Science* 149.3689, 1241–1242.

Spreiter, J., A. Summers, and A. Rizzi (1970). "Solar wind flow past nonmagnetic planets –Venus and Mars." In: *Planet. Space Sci.*

Squyres, S. W., R. E. Arvidson, S. Ruff, R. Gellert, R. V. Morris, D. W. Ming, ..., and P. A. de Souza Jr (2008). "Detection of silica-rich deposits on Mars." In: *Science* 320.5879, pp. 1063–1067.

Steckiewicz, M., P. Garnier, N. André, D. L. Mitchell, L. Andersson, E. Penou, ..., and B. M. Jakosky (2017). "Comparative study of the Martian suprathermal electron depletions based on Mars Global Surveyor, Mars Express, and Mars Atmosphere and Volatile EvolutioN mission observations." In: *Journal of Geophysical Research: Space Physics* 122.1, pp. 857–873.

Szegö, K., K. H. Glassmeier, R. Bingham, A. Bogdanov, C. Fischer, G.and ... Haerendel, and G. Zank (2000). "Physics of mass loaded plasmas." In: *Space Science Reviews* 94.3, pp. 429–671.

Tatrallyay, M., G. Gevai, I. Apathy, K. Schwingenschuh, T. L. Zhang, G. A. Kotova, ..., and H. Rosenbauer (1997). "Magnetic field overshoots in the Martian bow shock." In: *Journal of Geophysical Research: Space Physics* 102.A2, pp. 2157–2163.

Vignes, D., M. H. Acuña, J. E. P. Connerney, D. H. Crider, H. Reme, and C. Mazelle (2002). "Factors controlling the location of the Bow Shock at Mars." In: *Geophysical research letters* 29.9, pp. 42–1.

Vignes, D, C Mazelle, H Rme, and et al. (2000). "The solar wind interaction with Mars: Locations and shapes of the Bow Shock and the Magnetic Pile-up Boundary from the observations of the MAG/ER experiment onboard Mars Global Surveyor." In: *Geophysical Research Letters* 27.1, pp. 49–52.

Watson, C. C., P. K. Haff, and T. A. Tombrello (1980). "Solar wind sputtering effects in the atmospheres of Mars and Venus." In: *Lunar and Planetary Science Conference* 11, pp. 2479–2502.

Wu, X.-S., J. Cui, S. S. Xu, R. J. Lillis, R. V. Yelle, N. J. T. Edberg, and et al. (2019). "The morphology of the topside Martian ionosphere: Implications on bulk ion flow." In: *Journal of Geophysical Research: Planets* 124, 734–751.

Zhang, Q., H. Gu, J. Cui, Y. M. Cheng, Z. G. He, J. H. Zhong, ..., and Y. Wei (2020). "Atomic oxygen escape on Mars driven by electron impact excitation and ionization." In: *The Astronomical Journal* 159.2, p. 54.